

Effects of chaotic energy-band transport on the quantized states of ultracold sodium atoms in an optical lattice with a tilted harmonic trap

R. G. Scott, S. Bujkiewicz,* T. M. Fromhold, P. B. Wilkinson, and F. W. Sheard

School of Physics and Astronomy, University of Nottingham, Nottingham NG7 2RD, United Kingdom

(Received 18 October 2001; published 20 August 2002)

We investigate the classical and quantum properties of ultracold sodium atoms in a one-dimensional optical lattice and a three-dimensional harmonic trap. The energy versus crystal momentum dispersion relation for the lowest energy band of the optical lattice, together with the harmonic potential, define an effective Hamiltonian that we use to calculate classical atom paths. When one of the symmetry axes of the harmonic trap is aligned with the optical lattice, the atoms follow stable trajectories. But tilting this symmetry axis away from the optical lattice direction creates an unusual type of mixed stable-chaotic classical dynamics, which originates from the intrinsically quantum-mechanical nature of energy bands. In this regime, the density of quantized energy levels for the system exhibits periodic fluctuations associated with both stable and unstable periodic classical orbits. One of the unstable orbits also produces well-defined scar patterns in a subset of eigenfunctions. Wave functions with distinct spatial forms are identified and related directly to particular parts of the classical phase space using a Wigner function analysis.

DOI: 10.1103/PhysRevA.66.023407

PACS number(s): 32.80.Pj, 03.65.Sq, 05.45.Mt, 05.60.Cd

I. INTRODUCTION

The dynamics of particles in a periodic potential have been explored in a series of recent experiments and theoretical studies of noninteracting alkali-metal atoms [1–12] and Bose-Einstein condensates [13–20] in optical lattices (OLs) [21] formed by using two counterpropagating laser beams to set up an electromagnetic standing wave. The laser beams produce a periodic time-independent potential and an energy-band structure for atoms that are cold enough ($\leq 1 \mu\text{K}$) for their de Broglie wavelength to extend across several lattice periods. Detuning the lasers exerts an inertial force on the atoms, directed along the axis of the OL and of magnitude proportional to the rate of detuning [1]. Provided that this force is constant and weak enough to preserve the energy-band structure, atoms confined to a single band perform semiclassical Bloch oscillations [22]. In contrast to electrons in crystal lattices, the atoms undergo almost no scattering during the Bloch period, which is typically a few milliseconds [1], and the optical potential can be switched off rapidly at any time. This allows velocity-time curves for the Bloch oscillations to be measured directly in experiment [1], and makes OLs ideal for studying classical energy-band transport.

In a full quantum-mechanical picture, the atom energy associated with motion along the OL is quantized into a Wannier-Stark ladder [2–4] comprising equally spaced energy levels, which correspond to quantizing the action of the classical Bloch oscillations. Wannier-Stark ladders have been observed for ultracold sodium atoms in an accelerating OL whose phase is periodically modulated in order to drive interband transitions [2,3]. Since OLs can be used to investi-

gate directly both classical energy-band transport *and* the corresponding quantized states, they are well suited to experimental studies of the classical-quantum correspondence. This feature of OLs is particularly important in the field of quantum chaos: the study of quantum systems with chaotic classical analogs [23]. For example, the first experimental realization of a quantum δ -kicked rotor, which has served as a model system for the study of quantum chaos for many years [23], was achieved using ultracold atoms in phase-modulated OLs [5–12]. Cold ions in a Paul trap with a standing-wave laser field have also been shown to exhibit interesting chaotic dynamics [24,25].

In recent work, we investigated the classical motion of cold cesium atoms in the lowest energy band of an OL and confined by a three-dimensional harmonic trap [26]. When one of the symmetry axes of the trap is aligned with the propagation direction of the laser beams, the atoms follow regular classical paths. But tilting the symmetry axis away from this direction induces a transition from stable regular motion to mixed stable-chaotic dynamics [26]. An OL with a tilted harmonic trap therefore provides a different type of quantum chaotic system, in which the chaotic classical dynamics originate from an intrinsically quantum-mechanical property of the OL: its energy bands. Similar dynamics have been reported for electrons in a semiconductor superlattice with a tilted magnetic field [27]. But, to our knowledge, the quantized states corresponding to chaotic classical energy-band transport have not yet been studied.

In this paper, we investigate the quantized states of sodium atoms [28] in an OL with a tilted harmonic trap whose frequencies are low enough to preserve the band structure. We show that the onset of chaotic motion for atoms confined to the lowest energy band produces periodic fluctuations in the density of quantized energy levels, which we associate with both stable and unstable periodic classical paths. The wave functions corresponding to subsets of energy levels embedded within the full spectrum exhibit strong “scarring”: a concentration of probability density along an un-

*Permanent address: Institute of Physics, Wrocław University of Technology, Wybrzeże Wyspińskiego 27, 50-370 Wrocław, Poland.

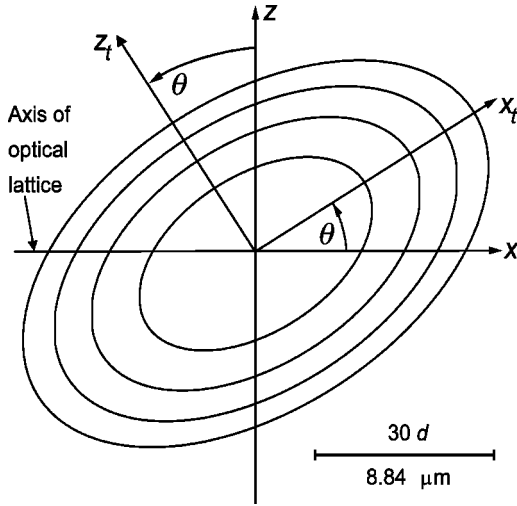


FIG. 1. Schematic diagram showing orientation of the OL and tilted harmonic trap. Ellipses show contours of potential energy in the x - z plane for a sodium atom confined by a harmonic trap with symmetry axes parallel to the x_t and z_t directions. The contours range from 10 to 40 peV at 10 peV intervals. The x_t symmetry axis of the harmonic potential is tilted at an angle θ to the x axis and laser field. Horizontal line indicates scale.

stable periodic orbit [29]. We relate the eigenstates of the system directly to the classical phase space structure by using a Wigner function analysis [30]. There is a striking similarity between the form of the atomic Wigner functions and the corresponding classical Poincaré sections. We also consider how the classical and quantum properties of the OL system might be explored in experiments on both individual atoms and Bose-Einstein condensates.

II. DESCRIPTION OF THE SYSTEM

We investigated the motion of cold noninteracting sodium atoms in a one-dimensional OL formed by two counterpropagating laser beams of wavelength λ aligned with the x axis (Fig. 1). The potential energy of a sodium atom in the OL is taken to be $U(x) = U_0 \sin^2(\pi x/d)$, where $d = \lambda/2 = 294.5$ nm and $U_0 = 562.52$ peV, as in recent experiments [3]. The form of $U(x)$ is shown by the solid curve in Fig. 2(a). A magnetically induced three-dimensional harmonic trap provides an additional confining potential. The equipotential surfaces of this trap are ellipsoids with three symmetry axes. In our coordinate system, one of these axes is parallel to the y direction and the other two (the x_t and z_t axes) lie in the x - z plane at an angle θ to the x and z axes (see Fig. 1). The potential energy of an atom in the harmonic trap is $V_T(x, y, z) = \frac{1}{2} m_a \omega_2^2 y^2 + V(x, z)$, where $V(x, z) = \frac{1}{2} m_a (\omega_1^2 x_t^2 + \omega_3^2 z_t^2)$, m_a is the mass of the sodium atom, $x_t = x \cos \theta + z \sin \theta$, $z_t = z \cos \theta - x \sin \theta$ (see Fig. 1), and the angular frequencies $\omega_1 = 1479$ rad s $^{-1}$, $\omega_2 = 4702$ rad s $^{-1}$, and $\omega_3 = 2561$ rad s $^{-1}$ are taken from experiments on sodium atoms in the $F = 1$, $M_F = -1$ state [31,32]. The closed ellipses in Fig. 1 show equipotential curves of $V(x, z)$ for $\theta = 30^\circ$.

Motion in the harmonic potential along the y direction is separable from that in the x - z plane, which is described by

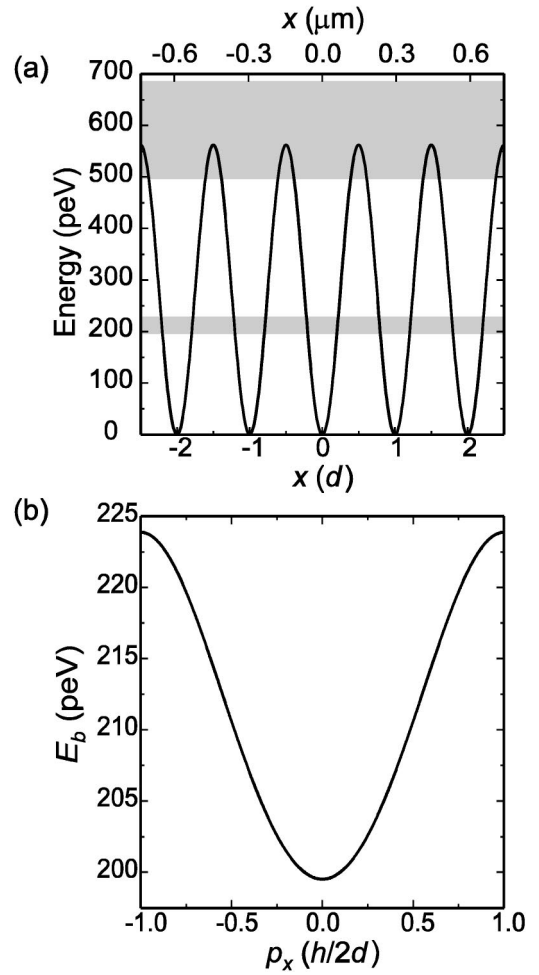


FIG. 2. (a) Solid curve shows potential energy $U(x)$ of a sodium atom in the OL. Gray rectangles show energy ranges of the first and second energy bands of the OL. (b) $E_b(p_x)$ dispersion relation calculated for the first energy band.

the time-independent Schrödinger equation

$$\left(\frac{\hat{p}_x^2 + \hat{p}_z^2}{2m_a} + V(x, z) + U(x) \right) \psi_n(x, z) = E_n \psi_n(x, z), \quad (1)$$

where \hat{p}_x , \hat{p}_z are momentum operators, E_n ($n = 1, 2, 3, \dots$) is a quantized energy eigenvalue for (x, z) motion, and $\psi_n(x, z)$ is the corresponding eigenfunction. In the next section, we use Eq. (1) to derive an effective classical Hamiltonian for atom orbits in the x - z plane and investigate the transition to chaotic classical dynamics induced by tilting the harmonic trap.

III. EFFECTIVE CLASSICAL HAMILTONIAN

In the absence of the harmonic trap, the OL potential produces energy bands for motion along the x direction. The gray bands in Fig. 2(a) indicate the energy ranges of the two lowest energy bands [3]. In this paper, we consider the motion of atoms confined to the first energy band at microkelvin temperatures. Figure 2(b) shows the dispersion curve of energy E_b versus crystal momentum p_x for this band, calcu-

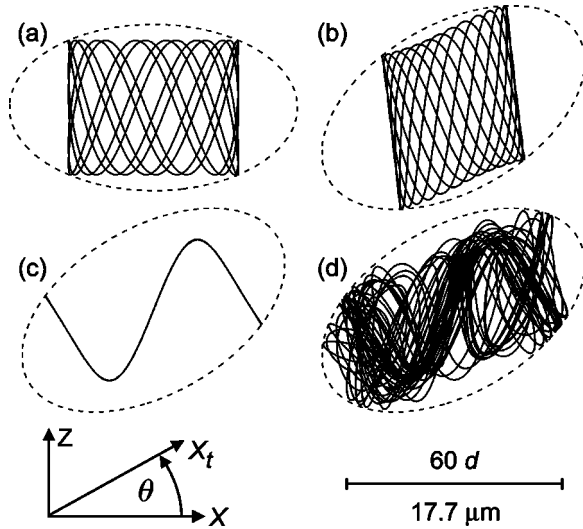


FIG. 3. Classical orbits in the x - z plane calculated for atoms in the first energy band of the OL with total energy $H=235.8$ peV and $\theta=0^\circ$ (a) and 30° (b)–(d). Orbits (c) and (d) both start from rest but with slightly different initial positions. Axes inset show orientation of symmetry axis x_t of the harmonic trap relative to the (x) axis of the laser field. Horizontal line indicates scale.

lated using Mathieu functions [33]. Without the harmonic trap, the total energy of an atom in the lowest energy band is $E(p_x, p_z) = E_b(p_x) + p_z^2/2m_a$, where p_z is the kinetic momentum associated with motion along the z direction. The translational symmetry of the OL, which leads to the formation of the energy bands, is broken when the harmonic trap is switched on. However, the trap frequencies ω_1 and ω_3 considered here are so low that within the region of space accessible to the atoms, the harmonic potential energy variation across a single period of the OL is much smaller than the width of the lowest energy band. Consequently, the harmonic potential can be treated as a perturbation to the OL potential, which induces transitions between the OL band states. Time-dependent perturbation theory shows that the harmonic potential continuously changes the average crystal momentum of the atom, thereby causing it to move through the energy band of the unperturbed OL [22]. The rate of change of the crystal momentum is $d\mathbf{p}/dt = -\nabla V$, where $\mathbf{p} = (p_x, p_z)$, and the mean atom velocity $\mathbf{v} = dE/d\mathbf{p}$. These two semiclassical equations of motion are well known in condensed matter physics [22]. They are equivalent to Hamilton's equations for an atom with an effective classical Hamiltonian given by

$$H(x, z, p_x, p_z) = E_b(p_x) + \frac{p_z^2}{2m_a} + V(x, z). \quad (2)$$

Since the harmonic trap is weak and the gap between the first and second energy bands is large [approximately 275 peV, Fig. 2(a)], interband transitions can be neglected.

IV. CLASSICAL ATOM DYNAMICS

Figure 3 shows real-space classical trajectories in the x - z plane calculated for an atom in the lowest energy band with

total energy $H=235.8$ peV. When $\theta=0^\circ$ [Fig. 3(a)], the Hamiltonian for motion in the x - z plane is separable and the atom undergoes simple harmonic motion along the z direction. Along the x axis, the harmonic potential accelerates the atom through the energy band, which also produces stable periodic motion [26]. When $\theta \neq 0^\circ$, the motion along the x and z directions is coupled and the orbital paths must be calculated by solving Hamilton's equations numerically. We used a fourth-order Runge-Kutta method to obtain solutions that remain accurate over time scales orders of magnitude longer than the inverse trap frequencies. Our calculations show that when $\theta \neq 0^\circ$ there are two distinct types of orbit whose form and stability depend on the initial conditions. One type of orbit is shown in Fig. 3(b) for $\theta=30^\circ$. This orbit resembles the simple regular motion found for $\theta=0^\circ$ [Fig. 3(a)]. It is stable in the sense that a small change in the initial conditions produces no qualitative change in the form of the trajectory. By contrast, the periodic orbit shown in Fig. 3(c) for $\theta=30^\circ$ is extremely unstable because an arbitrarily small change in the initial conditions causes the atom path to deviate rapidly from the periodic orbit, and thereafter follow a highly irregular path like that shown in Fig. 3(d).

To quantify how the atom motion changes with the trap orientation, Fig. 4 shows Poincaré sections, which display slices through the classical phase space [23], calculated for a range of θ values between 0° and 90° . The scattered points show the coordinate z and the corresponding momentum component p_z at each turning point along the x direction for which $p_x=0$ and $dp_x/dt < 0$. For $\theta=0^\circ$ and 90° [Figs. 4(a) and 4(f)], these points lie on a series of concentric ellipses corresponding to simple harmonic motion along the z direction. For intermediate tilt angles, the system is characterized by a rich stable-chaotic classical phase space [Figs. 4(b)–4(e)]. Toward the left-hand sides of the Poincaré sections in Figs. 4(b) and 4(c), calculated for $\theta=15^\circ$ and 30° , respectively, there are crescent-shaped stable islands, comprising a series of nested invariant curves [23] produced by regular orbits like that shown in Fig. 3(b). Crescents further from the centers of these stable islands are more strongly curved. Near the boundary with the chaotic seas in Figs. 4(b) and (c), the crescents are so strongly curved that their tips almost touch, but remain separated by a hyperbolic fixed point, which corresponds to an unstable orbit. The crescent-shaped islands enclose the chaotic seas in Figs. 4(b) and 4(c), which themselves contain additional stable islands. When θ is increased to 45° [Fig. 4(d)], the additional islands disappear. Raising θ to 60° [Fig. 4(e)] increases the size of the chaotic sea, which now encloses all of the stable islands. As θ is increased beyond 60° , these stable islands grow and there is a gradual transition to the completely regular phase space found for $\theta=90^\circ$ [Fig. 4(f)].

We emphasize that the classical phase space structure has an intrinsically quantum-mechanical origin associated with the energy-band structure. Due to the different energy-momentum dispersion relations for motion parallel and perpendicular to the axis of the OL, the atoms have an anisotropic and energy-dependent effective mass. When the harmonic trap is tilted relative to the OL, this anisotropy couples the motion along the x and z directions and thereby

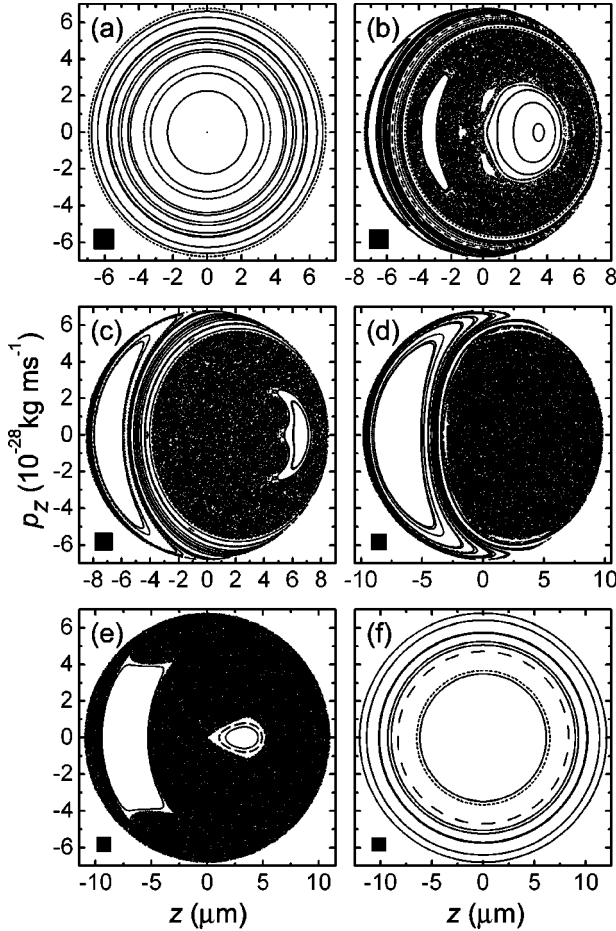


FIG. 4. Poincaré sections (z, p_z) through the classical phase space calculated for atoms in the first energy band of the OL with $\theta=0^\circ$ (a), 15° (b), 30° (c), 45° (d), 60° (e), and 90° (f). Each section is constructed from 220 different trajectories with $H = 237.3$ peV. Areas of black squares equal \hbar .

induces mixed stable-chaotic dynamics. We have found that similar dynamics occur for a wide range of system parameters and atom energies, and also for other alkali-metal atoms [26].

A similar type of chaotic energy-band transport has recently been demonstrated for electrons in a semiconductor superlattice with a tilted magnetic field [27]. In this condensed matter system, the onset of chaos can only be detected by investigating its effect on the current-voltage characteristics of the superlattice. By contrast, for the atomic system considered here, the classical trajectories could be observed directly in time-resolved transport experiments similar to those used to detect Bloch oscillations for cesium atoms [1]. Moreover, since the initial positions and velocities of the atoms are well defined and can be precisely controlled [1,34,35], such experiments might also be used to map out Poincaré sections for chaotic energy-band transport in the present system. The black squares in Fig. 4 show the fundamental phase space resolution limit of \hbar which is, in principle, fine enough to allow experimental detection of the stable islands. It is now possible to prepare cold atoms in

minimum-uncertainty Gaussian initial states whose position-momentum spread is at this limit [34,35].

V. QUANTIZED ENERGY LEVEL SPECTRUM AND EIGENSTATES OF THE ATOMS

To investigate how the onset of classical energy-band transport affects the quantized states of the system, we calculated the eigenvalues E_n and corresponding eigenfunctions $\psi_n(x, z)$ of Eq. (1). We expanded the eigenfunctions

$$\psi_n(x, z) = \sum_{l,r} c_{l,r}^n f(x-x_l) \Phi_r(z), \quad (3)$$

over a basis comprising Wannier functions $f(x-x_l)$ for the first energy band, where x_l is the position of the l th minimum in $U(x)$, and the eigenfunctions $\Phi_r(z)$ ($r=0,1,2,3,\dots$) of a simple harmonic oscillator of angular frequency ω_3 , centered at $z=0$. The Wannier functions used in our calculations are given by [36]

$$f(x-x_l) = \frac{d}{h} \int_{-h/2d}^{h/2d} \exp(ip_x x_l / \hbar) u_{p_x}(x) dp_x,$$

where $u_{p_x}(x)$ is the Bloch function corresponding to crystal momentum p_x in the first energy band. The Bloch functions are obtained by numerical solution of Mathieu's equation [33]. In this basis, the Hamiltonian Eq. (1) reduces to a banded real symmetric matrix whose eigenvalues are the energy levels E_n . Here, we analyze the energy level spectrum and eigenfunctions for the tilt angle $\theta=30^\circ$ corresponding to the mixed stable-chaotic phase space shown in Fig. 4(c). Eigenstates for other system parameters corresponding to mixed stable-chaotic dynamics have similar properties.

The horizontal lines in Fig. 5 show the quantized energy levels in the range 235.3 peV $\leq E_n \leq 237.6$ peV. Over this energy range, the classical phase space structure is almost identical to that shown in Fig. 4(c). The energy level spectrum exhibits the complex aperiodic distribution characteristic of nonintegrable systems [23]. Despite this complexity, two distinct features of the spectrum can be related directly to the classical motion of an atom in the lowest energy band: the number of energy levels $N(E)$ below a particular energy E , and long-range periodic fluctuations in the level density. We now analyze each of these features in turn.

The number of energy levels below energy E is given by the staircase function

$$N(E) = \sum_n \Theta(E - E_n), \quad (4)$$

where $\Theta(E - E_n)$ is the step function of unit height. The solid curve in Fig. 6(a) shows $N(E)$ for the lowest 20 energy levels. The curve contains stepped oscillatory structure, which originates from the energy quantization, superimposed on a monotonically increasing background. We can therefore express $N(E)$ as the sum of a rapidly fluctuating step function $N_{OS}(E)$ and a slowly varying ‘‘Weyl’’ [23] term $N_{AV}(E)$, which gives the average number of energy levels

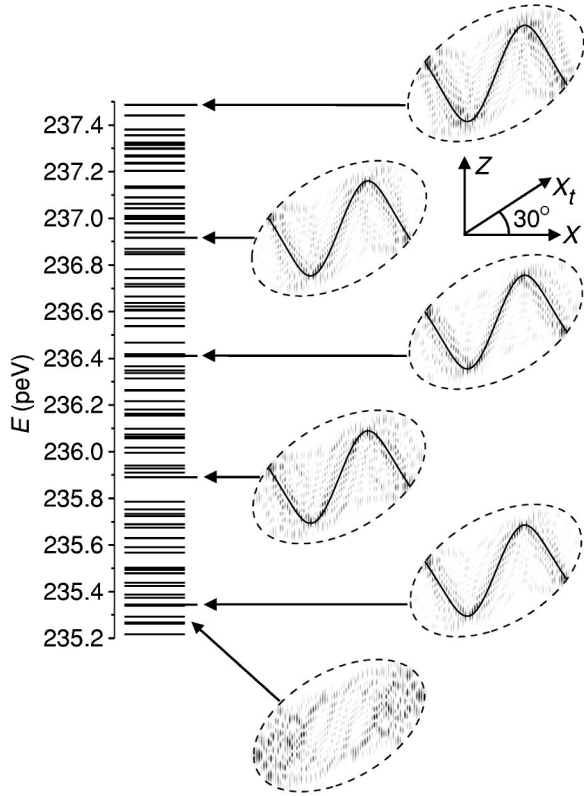


FIG. 5. Horizontal lines: energy eigenvalues for a sodium atom in the system with $\theta=30^\circ$. Longer lines mark the energies of the scarred energy eigenfunctions shown on the right of the figure (top five plots) with spatial axes inset. The S-shaped unstable periodic orbits (black curves) are overlaid on the probability density plots (white = 0, black = high) of each scarred mode. The probability distribution of an unscarred mode (bottom plot) is shown for comparison. In each wave function plot, the dashed ellipse shows the equipotential energy curve of the harmonic trap defined by $V(x, z) = E_n - E_b(0)$.

below E . We have calculated the Weyl term from the Hamiltonian Eq. (2) for classical energy-band transport using the formula [23]

$$N_{AV}(E) = \frac{1}{h^2} \int \int \int \int \Theta(E - H(x, z, p_x, p_z)) \times dp_x dp_z dx dz, \quad (5)$$

where the integrals are over the classically allowed region of phase space at energy E . Analytical expressions for the integrals over x , z , and p_z reduce Eq. (5) to

$$N_{AV}(E) = \left(\frac{2}{m_a}\right)^{1/2} \frac{4}{3\pi(\hbar\omega_1)(\hbar\omega_3)} \times \int_0^{h/2d} [E - E_b(p_x)]^{3/2} dp_x, \quad (6)$$

where the integral over p_x must be evaluated numerically since $E_b(p_x)$ is not a simple function. The dashed curve in Fig. 6(a) shows $N_{AV}(E)$. Even though this curve is derived

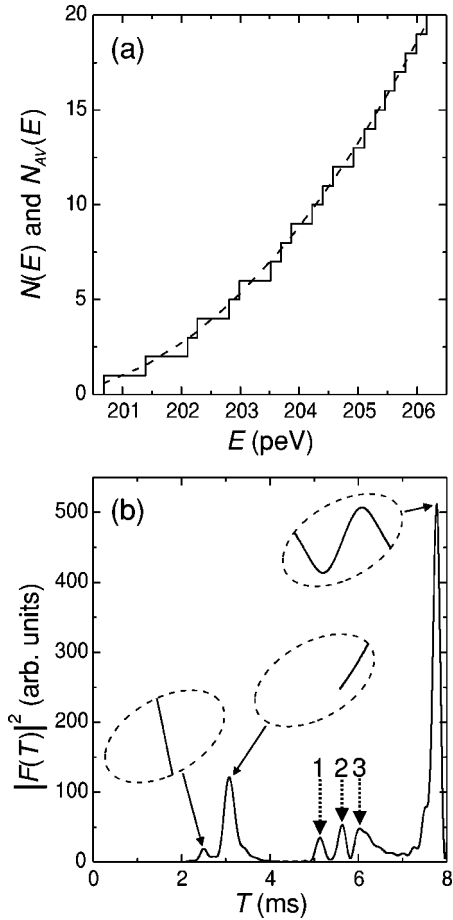


FIG. 6. (a) $N(E)$ (solid curve) and $N_{AV}(E)$ (dashed curve) plots calculated for $\theta=30^\circ$. (b) Fourier power spectrum of $D_{OS}(E)$ in the range $224.6 \text{ peV} \leq E \leq 247.1 \text{ peV}$, shown as a function of time T . Inset: periodic atom orbits corresponding to the peaks marked by solid arrows. Ellipses show the equipotential energy curve of the harmonic trap defined by $V(x, z) = E - E_b(0)$, with $E = 237.3 \text{ peV}$. The origin of peaks 1–3 (dotted arrows) is discussed in the text.

from an effective classical Hamiltonian Eq. (1), it gives a good approximation to the $N(E)$ staircase function obtained from full quantum-mechanical calculations. This supports our claim in Sec. III, that a classical picture of energy-band transport is valid because V is a slowly varying function of x and z .

The density of quantized energy levels is given by

$$D(E) = \frac{dN(E)}{dE} = D_{AV}(E) + D_{OS}(E), \quad (7)$$

where $D_{AV}(E) = dN_{AV}(E)/dE$ is a smooth monotonically increasing average level density and $D_{OS}(E) = dN_{OS}(E)/dE$ is the remaining fluctuating contribution. In the semiclassical limit, $D_{OS}(E)$ can be related to the periodic classical orbits of the system using the trace formula [23]

$$D_{OS}(E) = \text{Im} \sum_j a_j \exp[iS_j(E)/\hbar], \quad (8)$$

where $S_j(E)$ is the classical action of the j th orbit, and the expansion coefficients a_j depend on the orbital stability. Each periodic orbit imposes a regular modulation in $D_{OS}(E)$ with an energy period $\Delta E_j = h[dS_j(E)/dE]^{-1} = h/T_j(E)$, where $T_j(E)$ is the period of the j th orbit. To identify the periodic fluctuations in $D_{OS}(E)$ and the associated classical orbits, we calculated the Fourier transform

$$F(T) = \int_0^{E_m} D_{OS}(E) G(E) \exp(-iET/\hbar) dE, \quad (9)$$

where E_m is the highest eigenvalue considered and $G(E)$ is the Welch window function, which we use to suppress ringing in the Fourier transform [37,38].

The power spectrum of $F(T)$ shown in Fig. 6(b) reveals three peaks (marked by solid arrows) at times T equal to the periods of the three distinct periodic classical orbits shown inset in the figure. The orbits corresponding to the two leftmost peaks are stable, while that associated with the right-hand peak is unstable. The dotted arrows in Fig. 6(b) indicate three additional peaks, labeled 1–3, in the range $5 \text{ ms} \leq T \leq 6 \text{ ms}$. Peaks 1 and 3 are harmonics of the maxima at $T \approx 2.5$ and 3 ms , respectively, which are marked by the two leftmost solid arrows in Fig. 6(b). There is no periodic orbit corresponding to peak 2, which probably originates from complex “ghost” trajectories [39–41] like those previously identified for electrons in hydrogenic atoms [39,41] and light in chaotic optical cavities [37,38].

We also investigated the relation between the classical orbits and quantized eigenfunctions of the system. Many of the wave functions reflect the diffuse irregular forms of the chaotic classical paths such as the one shown in Fig. 3(d). For example, the probability density plot for the bottom wave function in Fig. 5 has a highly complex antinode pattern. Just like the chaotic classical paths, this wave function extends throughout the classically allowed region bounded by the dashed ellipse which shows the equipotential $V(x,z) = E_n - E_b(0)$ of the harmonic trap. By contrast, the wave functions corresponding to regular subsets of energy levels embedded in the complete spectrum are strongly localized or “scarred” along unstable but periodic classical paths [29]. For example, the wave functions corresponding to the energy levels marked by the longer horizontal lines in Fig. 5 all exhibit clear scars of the S-shaped unstable periodic orbit shown overlaid and also in Fig. 3(c). The wave functions pertaining to energy levels between these scarred states generally reveal no trace of the scar pattern. Adjacent scarred states in Fig. 5 are separated by an energy of $\approx 0.53 \text{ peV}$, which equals the value of h/T_S obtained from the period $T_S \approx 7.8 \text{ ms}$ of the S-shaped orbits.

Subsets of scarred wave functions also occur for electrons in hydrogenic atoms [42], in the quantum well of semiconductor resonant tunneling diodes (RTDs) [43–45], and for the electromagnetic eigenmodes of analogous gradient refractive index optical cavities [37,38]. In the RTDs, the scarred states control the rates of tunneling transitions into the quantum well, and thereby generate pronounced resonant peaks in current versus voltage measurements [44]. It might be possible to detect the sequence of scarred states in the

atomic system considered here by using phase modulation of the OL to induce interstate transitions and determine the probability of excitation [2–4]. We expect that the large spatial overlap between adjacent scarred states would produce strong resonant transitions when the modulation frequency equals $2\pi/T_S$. Such experiments might also provide information about fluctuations of the density of levels and about the statistics of nearest-neighbor level spacings, which follow the Brody distribution [46] for systems with mixed stable chaotic dynamics.

VI. WIGNER FUNCTION ANALYSIS OF THE EIGENSTATES: LINKS WITH THE CLASSICAL PHASE SPACE

To relate the quantized states of the system directly to the corresponding classical phase space, for each eigenfunction $\psi_n(x,z)$ we calculated the Wigner function [30]

$$\begin{aligned} W_n(x,z,p_x,p_z) &= \frac{1}{h^2} \int_{-\infty}^{\infty} \int_{-\infty}^{\infty} \psi_n^* \left(x + \frac{\lambda_x}{2}, z + \frac{\lambda_z}{2} \right) \\ &\quad \times \psi_n \left(x - \frac{\lambda_x}{2}, z - \frac{\lambda_z}{2} \right) \\ &\quad \times \exp[-i(p_x \lambda_x + p_z \lambda_z)/\hbar] d\lambda_x d\lambda_z, \end{aligned} \quad (10)$$

where λ_x and λ_z are real variables. We reduced W_n to a two-dimensional function of z and p_z in the following way. First, in Eq. (10), we set $p_x = 0$, so that the Wigner functions are calculated over the same phase space plane as the classical Poincaré sections shown in Fig. 4. For this particular p_x and specified phase space components (z, p_z) , the value of x used in Eq. (10) is determined uniquely [47] by E_n and the form of the classical Hamiltonian $H = E_n$ given in Eq. (2) [48]. The two-dimensional Wigner functions $W_n(z, p_z)$ give a phase space representation of the eigenfunctions, and are analogous to classical Poincaré sections [30,37,38]. Figure 7 shows $W_n(z, p_z)$ calculated for the wave function in the middle ($E_n \approx 236.45 \text{ peV}$) of the sequence of scarred states in Fig. 5. This Wigner function is the quantum analog of the Poincaré section shown in Fig. 4(c). To help relate the Wigner function to the Poincaré section, the dotted curves in Fig. 7 show the perimeters of the two large stable islands in Fig. 4(c). The large absolute values of W_n (white and black regions) are centered on the point (z_S, p_{zS}) (marked by the cross, which lies within the chaotic sea) where the scarring S-shaped orbit crosses the $p_x = 0$ plane with $dp_x/dt < 0$. This provides further evidence that the scar pattern originates from the S-shaped orbit.

In Fig. 8, we use Wigner functions to relate wave functions with distinct spatial forms to particular regions of the classical phase space. The plots on the left-hand side of the figure show the probability density distributions of four different eigenfunctions, and those on the right-hand side show the corresponding Wigner functions. At the energy corresponding to each eigenfunction, the classical Poincaré section is almost identical to that shown in Fig. 4(c). The perimeters of the two large stable islands in this Poincaré

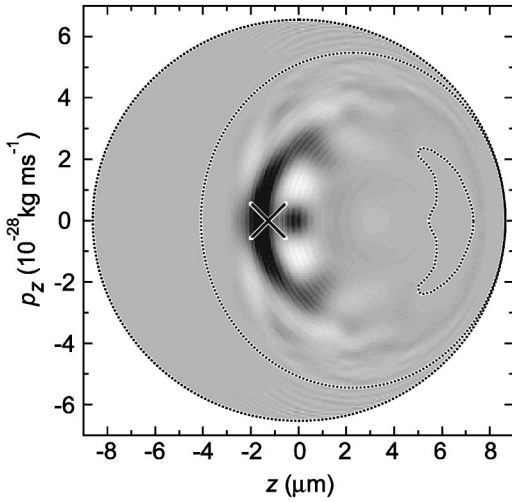


FIG. 7. Wigner function $W_n(z, p_z)$ (black $\ll 0$, gray = 0, white $\gg 0$) corresponding to the third scarred wave function from the top in Fig. 5. Cross indicates the point where the S-shaped scarring orbit crosses the $p_x = 0$ plane with $dp_x/dt < 0$. Dotted curves show perimeters of the two large stable islands in Fig. 4(c).

section are shown by the dotted curves superimposed on the Wigner functions in Fig. 8. In Fig. 8(a), the wave function is localized along the overlaid stable linear periodic orbit, which lies at the center of the left-hand crescent-shaped stable island in Fig. 4(c). The corresponding Wigner function is concentrated around this center point [marked by the cross in Fig. 8(a)], where the linear orbit crosses the $p_x = 0$ plane with $dp_x/dt < 0$. Its form echoes some of the innermost crescent-shaped invariant curves in the left-hand stable island of Fig. 4(c). The wave function in Fig. 8(b) is localized along the two overlaid stable periodic paths, which reflect the symmetry of the system under a 180° rotation. At the outer turning points of these orbits, the atoms paths are bounded by the dashed equipotential of the harmonic trap. By contrast, the inner turning points originate from the effect of the OL energy band structure on the atom motion. These turning points occur when the atom's crystal momentum $p_x = \pm h/2d$ is at the edge of the first Brillouin zone, where the gradient of the dispersion curve $E_b(p_x)$ is zero [Fig. 2(b)]. Consequently, the mean velocity of the atom is also zero and so there is a turning point in the classical motion along the x direction. In a fully quantum-mechanical picture, the atom is stationary at the edges of the Brillouin zone because its wave function is Bragg reflected by the OL and therefore takes the form of a standing wave. The right-hand orbit in Fig. 8(b) lies at the center of the right-hand stable island in Fig. 4(c), which is marked by the cross in the Wigner function of Fig. 8(b). This Wigner function is concentrated within the right-hand stable island and has maximal amplitude at its center point. The left-hand orbit in Fig. 8(b) does not appear in either the Poincaré section or the Wigner function, since when $p_x = 0$ along this orbit, $dp_x/dt > 0$ [47]. In Fig. 8(c), the wave function is concentrated within the caustics of the overlaid stable orbit, which lies near the perimeter of the left-hand stable island in Fig. 4(c). The Wigner function in Fig. 8(c) extends throughout the left-hand stable island,

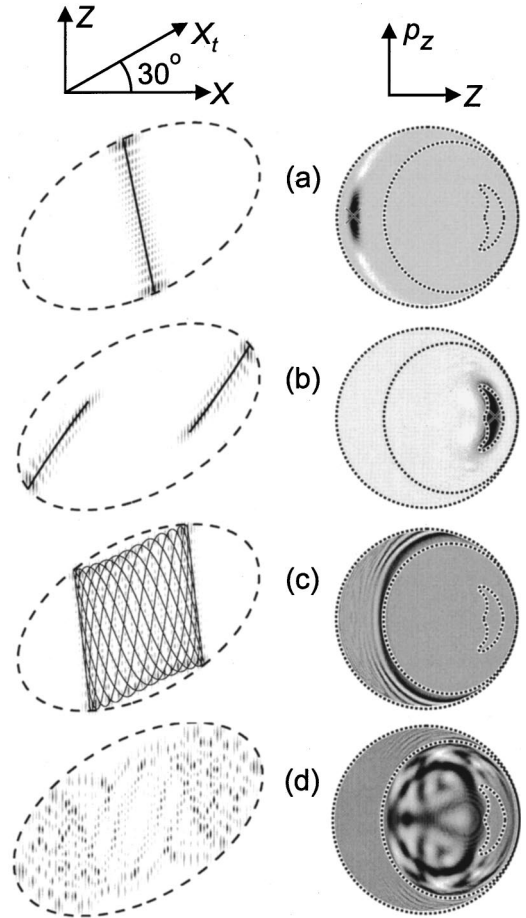


FIG. 8. Left: probability density plots in the x - z plane (coordinate axes shown top left) for eigenstates of the system with $\theta = 30^\circ$ and $(n, E_n) = (670, 235.7 \text{ peV})$ (a), $(675, 235.9 \text{ peV})$ (b), $(674, 235.8 \text{ peV})$ (c), $(760, 238.0 \text{ peV})$ (d). Classical paths associated with wave functions (a)–(c) are overlaid. Right: the corresponding Wigner functions $W_n(z, p_z)$ (black $\ll 0$, gray = 0, white $\gg 0$) with coordinate axes shown top right. The coordinate ranges of the Wigner functions are $-9 \mu\text{m} < z < 9 \mu\text{m}$ and $-7 \times 10^{-28} \text{ kg ms}^{-1} < p_z < 7 \times 10^{-28} \text{ kg ms}^{-1}$, as in Fig. 4(c). Crosses in (a) and (b) indicate the points where the classical orbits shown on the left of the figure cross the $p_x = 0$ plane with $dp_x/dt < 0$. Dotted curves on Wigner function plots show perimeters of the two large stable islands in Fig. 4(c).

which suggests that the corresponding eigenfunction is associated with all of the orbits in this region of phase space, rather than a single periodic path. To conclude this section, we consider the irregular probability distribution shown in Fig. 8(d), whose Wigner function spreads throughout the chaotic sea in Fig. 4(c), but has almost zero amplitude within the stable islands bounded by the dotted curves in Fig. 8(d). The extended nature of this Wigner function shows that many different chaotic trajectories contribute to the wave function pattern, which accounts for its complex diffuse form.

VII. CONCLUSION

In summary, we have investigated the classical motion and quantized states of ultracold sodium atoms in an OL with

a harmonic trap. When a symmetry axis of the trap is tilted relative to the OL, the atoms exhibit an unusual type of chaotic motion determined by an effective classical Hamiltonian, which originates from the energy band dispersion. For the low trap frequencies considered here, the harmonic potential acts as a small slowly varying perturbation to the OL. Consequently, the atomic motion can be described by an effective classical Hamiltonian, Eq. (2), in which the energy-band structure of the unperturbed OL is supplemented by the harmonic trap potential. The periodic orbits of this Hamiltonian have a pronounced effect on the quantized eigenstates of the system. In particular, they modulate the density of energy levels and scar subsets of eigenstates. Both of these effects might be accessible to experimental study by using phase modulation of the OL to drive transitions between the first and second energy bands and thereby determine the probability of excitation [2,3]. The possibility of detecting both the classical trajectories and the quantized eigenstates, plus the large number of controllable parameters, makes the OL system particularly attractive for studying the dynamical

regime of chaotic energy-band transport [27].

Finally, we note that there is great current interest in the quantum properties of Bose-Einstein condensates in OLs [13–20]. Previous work has considered a one-dimensional OL aligned with a symmetry axis of a condensate in a harmonic trap [15,19]. For this geometry, numerical simulations [16,18] and experiments [14] show that the collective dynamics of a condensate in an accelerating OL are very similar to single-atom Bloch oscillations [1]. By analogy, we anticipate that the onset of chaos for single atoms in an OL with a tilted harmonic trap may also be manifest in the collective time-dependent dynamics and excitations of a condensate in this system.

ACKNOWLEDGMENTS

This work was supported by the U.K. Engineering and Physical Sciences Research Council (Grant No. GR/R41132/01) and NATO linkage Grant No. PST.CLG.97690.

-
- [1] M. Ben Dahan, E. Peik, J. Reichel, Y. Castin, and C. Salomon, *Phys. Rev. Lett.* **76**, 4508 (1996).
- [2] Qian Niu, Xian-Geng Zhao, G.A. Georgakis, and M.G. Raizen, *Phys. Rev. Lett.* **76**, 4504 (1996).
- [3] S.R. Wilkinson, C.F. Bharucha, K.W. Madison, Qian Niu, and M.G. Raizen, *Phys. Rev. Lett.* **76**, 4512 (1996).
- [4] M. Glück, M. Hankel, A.R. Kolovsky, and H.J. Korsch, *J. Opt. B: Quantum Semiclassical Opt.* **2**, 612 (2000).
- [5] F.L. Moore, J.C. Robinson, C. Bharucha, P.E. Williams, and M.G. Raizen, *Phys. Rev. Lett.* **73**, 2974 (1994).
- [6] J.C. Robinson, C. Bharucha, F.L. Moore, R. Jahnke, G.A. Georgakis, Qian Niu, M.G. Raizen, and B. Sundaram, *Phys. Rev. Lett.* **74**, 3963 (1995).
- [7] B.G. Klappauf, W.H. Oskay, D.A. Steck, and M.G. Raizen, *Phys. Rev. Lett.* **81**, 1203 (1998); **82**, 241 (1999).
- [8] H. Ammann, R. Gray, I. Shvarchuck, and N. Christensen, *Phys. Rev. Lett.* **80**, 4111 (1998).
- [9] W.H. Oskay, D.A. Steck, B.G. Klappauf, and M.G. Raizen, *Laser Phys.* **9**, 265 (1999).
- [10] W.H. Oskay, D.A. Steck, V. Milner, B.G. Klappauf, and M.G. Raizen, *Opt. Commun.* **179**, 137 (2000).
- [11] V. Milner, D.A. Steck, W.H. Oskay, and M.G. Raizen, *Phys. Rev. E* **61**, 7223 (2000).
- [12] K.M.D. Vant, G.H. Ball, and N. Christensen, *Phys. Rev. E* **61**, 5994 (2000).
- [13] K. Berg-Sørensen and K. Mølmer, *Phys. Rev. A* **58**, 1480 (1998).
- [14] B.P. Anderson and M.A. Kasevich, *Science* **282**, 1686 (1998).
- [15] D. Jaksch, C. Bruder, J.I. Cirac, C.W. Gardiner, and P. Zoller, *Phys. Rev. Lett.* **81**, 3108 (1998).
- [16] D.-I. Choi and Q. Niu, *Phys. Rev. Lett.* **82**, 2022 (1999).
- [17] K.P. Marzlin and Weiping Zhang, *Phys. Rev. A* **59**, 2982 (1999).
- [18] M. Holthaus, *J. Opt. B: Quantum Semiclassical Opt.* **2**, 589 (2000).
- [19] S. Burger, F.S. Cataliotti, C. Fort, F. Minardi, M. Inguscio, M.L. Chiofalo, and M.P. Tosi, *Phys. Rev. Lett.* **86**, 4447 (2001).
- [20] J.C. Bronski, L.D. Carr, B. Deconinck, and J.N. Kutz, *Phys. Rev. Lett.* **86**, 1402 (2001).
- [21] For a review, see D.R. Meacher, *Contemp. Phys.* **39**, 329 (1998).
- [22] The motion of atoms in an energy band is semiclassical because the effective classical equations of motion are derived by considering the response of a quantum-mechanical wave packet to force fields that are spatially slowly varying [see, for example, N. W. Ashcroft and N. D. Mermin, *Solid State Physics* (Holt, Rinehart, and Winston, New York, 1976), Chap. 12]. Henceforth, we refer to these equations of motion, and the trajectories that they produce, as simply classical.
- [23] For a review see H.-J. Stöckmann, *Quantum Chaos: An Introduction* (Cambridge University Press, Cambridge, England, 1999); L.E. Reichl, *The Transition to Chaos* (Springer-Verlag, New York, 1992).
- [24] M. El Ghafar, P. Törmä, V. Savichev, E. Mayr, A. Zeiler, and W.P. Schleich, *Phys. Rev. Lett.* **78**, 4181 (1997).
- [25] K. Riedel, P. Törmä, V. Savichev, and W.P. Schleich, *Phys. Rev. A* **59**, 797 (1999).
- [26] T.M. Fromhold, C.R. Tench, S. Bujkiewicz, P.B. Wilkinson, and F.W. Sheard, *J. Opt. B: Quantum Semiclassical Opt.* **2**, 628 (2000).
- [27] T.M. Fromhold, A.A. Krokhin, C.R. Tench, S. Bujkiewicz, P.B. Wilkinson, F.W. Sheard, and L. Eaves, *Phys. Rev. Lett.* **87**, 046803 (2001).
- [28] We consider sodium atoms, rather than the cesium atoms used in our previous work [26], because of their potential for future studies of Bose-Einstein condensates in an OL with a tilted harmonic trap.
- [29] E.J. Heller, *Phys. Rev. Lett.* **53**, 1515 (1984).
- [30] P.A. Dando and T.S. Monteiro, *J. Phys. B* **27**, 2681 (1994).

- [31] K.B. Davis, M.-O. Mewes, M.R. Andrews, N.J. van Druten, D.S. Durfee, D.M. Kurn, and W. Ketterle, *Phys. Rev. Lett.* **75**, 3969 (1995).
- [32] This form of harmonic potential assumes that all of the atoms have the same magnetic sublevel M_F . If there is a mixture of sublevels, all of the atoms follow qualitatively similar classical paths, but the details of the phase space structure depend on M_F .
- [33] *Handbook of Mathematical Functions*, edited by M. Abramowitz and I. A. Stegun (Dover, New York, 1970).
- [34] D.A. Steck, W.H. Oskay, and M.G. Raizen, *Science* **293**, 274 (2001).
- [35] W.K. Hensinger, H. Haffer, A. Browaeys, N.R. Heckenberg, K. Helmerson, C. McKenzie, G.J. Milburn, W.D. Phillips, S.L. Rolston, H. Rubinsztein-Dunlop, and B. Upcroft, *Nature (London)* **412**, 52 (2001).
- [36] A.M. Bouchard and M. Luban, *Phys. Rev. B* **52**, 5105 (1995).
- [37] P.B. Wilkinson, T.M. Fromhold, R.P. Taylor, and A.P. Micolich, *Phys. Rev. Lett.* **86**, 5466 (2001).
- [38] P.B. Wilkinson, T.M. Fromhold, R.P. Taylor, and A.P. Micolich, *Phys. Rev. E* **64**, 026203 (2001).
- [39] P. Bellomo and T. Uzer, *Phys. Rev. A* **51**, 1669 (1995).
- [40] A.M. Ozorio de Almeida and J.H. Hannay, *J. Phys. A* **20**, 5873 (1987).
- [41] T.S. Monteiro and P. Dando, *Phys. Rev. E* **53**, 3369 (1996).
- [42] D. Wintgen and A. Hönig, *Phys. Rev. Lett.* **63**, 1467 (1989).
- [43] T.M. Fromhold, P.B. Wilkinson, F.W. Sheard, L. Eaves, J. Miao, and G. Edwards, *Phys. Rev. Lett.* **75**, 1142 (1995).
- [44] P.B. Wilkinson, T.M. Fromhold, L. Eaves, F.W. Sheard, N. Miura, and T. Takamasu, *Nature (London)* **380**, 608 (1996).
- [45] E.E. Narimanov and A.D. Stone, *Phys. Rev. Lett.* **80**, 49 (1998).
- [46] T.A. Brody, *Lett. Nuovo Cimento Soc. Ital. Fis.* **7**, 482 (1973).
- [47] For given p_x , z , p_z , and E_n , the classical Hamiltonian Eq. (2) actually gives two possible values of x . We chose the one for which $dp_x/dt = -\partial H/\partial x < 0$, to ensure that the Wigner functions are calculated in the same way as the Poincaré sections described in Sec. IV, that is, crossing the $p_x=0$ plane in the direction for which $dp_x/dt < 0$.
- [48] We used the classical Hamiltonian Eq. (2) to determine the value of x in order to ensure that the Wigner functions shown in Figs. 7 and 8 are calculated over the *same* surface in phase space as the classical Poincaré sections shown in Fig. 4. This facilitates direct comparison of the classical and quantum results.